



# Pseudo-continuous arterial spin labeling MR images in Warthin tumors and pleomorphic adenomas of the parotid gland: qualitative and quantitative analyses and their correlation with histopathologic and DWI and dynamic contrast enhanced MRI findings

Tatsuya Yamamoto<sup>1,2</sup> · Hirohiko Kimura<sup>2</sup> · Kuniyoshi Hayashi<sup>3</sup> · Yoshiaki Imamura<sup>4</sup> · Masaki Mori<sup>4</sup>

Received: 6 September 2017 / Accepted: 4 June 2018 / Published online: 2 July 2018  
© Springer-Verlag GmbH Germany, part of Springer Nature 2018

## Abstract

**Purpose** We investigated the correlation between tumor blood flow (TBF) and histopathologic features of Warthin tumors (WTs) and pleomorphic adenomas (PAs) to determine the TBF in the differential diagnosis of these tumors and evaluated how well pCASL-MRI can differentiate PAs from WT compared to conventional MRI.

**Methods** The ADC, time intensity curve (TIC) pattern of dynamic contrast enhancement, and pCASL (visual assessment and TBF of the MR images of 10 WT and 13 PAs) were reviewed. We compared the pCASL and ADC or TIC patterns in WT and PA images. Tissue sections were stained with CD34 to evaluate microvessel density (MVD). The TBF and MVD results were compared. The Mann-Whitney *U* test was used to compare the TBFs, ADCs, and MVDs of these tumors. The diagnostic accuracy was determined by analyzing the receiver operating characteristic curve.

**Results** On visual assessment, the signal intensity was higher in all but three cases of WT. The TBF and MVD of the WT were significantly higher (both,  $p < 0.01$ ) than the PAs, and the ADC was significantly lower ( $p < 0.01$ ). Many WT had early enhancement of the TIC pattern and high washout; many PAs had gradual enhancement. The diagnostic accuracies of visual analysis, TBF, and ADC for differentiation between WT and PAs were 91.3, 95.7, and 87.0%, respectively.

**Conclusions** The TBF were significantly higher in WT than in PAs, and there was a positive correlation between TBF and MVD. Moreover, pCASL-MRI provides more accurate imaging than conventional MRI to differentiate WT and PAs.

**Keywords** Arterial spin labeling · Magnetic resonance imaging · Parotid gland tumor · Warthin tumor · Pleomorphic adenoma

The preliminary results of this study were presented at the Joint Annual Meeting and Exhibition of International Society for Magnetic Resonance in Medicine (ISMRM) and the European Society for Magnetic Resonance in Medicine and Biology (ESMRMB) on 13 May 2014, Milan, Italy.

✉ Hirohiko Kimura  
kimura\_hiro0@yahoo.co.jp

<sup>1</sup> Department of Diagnostic Radiology, The Cancer Institute Hospital of the Japanese Foundation for Cancer Research, 3-8-31 Ariake, Koto-ku, Tokyo 135-8550, Japan

<sup>2</sup> Department of Radiology, Faculty of Medical Sciences, University of Fukui, 23-3 Matsuoka-Shimoaizuki, Eiheiji-cho, Fukui 910-1193, Japan

<sup>3</sup> Division of Biostatistics and Bioinformatics, Graduate School of Public Health, St. Luke's International University, 3-6-2 Tsukiji, Chuo-ku, Tokyo 104-0045, Japan

<sup>4</sup> Division of Surgical Pathology, University of Fukui Hospital, 23-3 Matsuoka-Shimoaizuki, Eiheiji-cho, Fukui 910-1193, Japan

## Abbreviations

ADC	apparent diffusion coefficient
ASL	arterial spin labeling
AUC	area under the curve
CBF	cerebral blood flow
CNS	central nervous system
DWI	diffusion weighted image
EPI	echo-planar imaging
FOV	field of view
FSE	fast spin-echo
MRI	magnetic resonance imaging
MVD	microvessel density
NEX	number of excitation
NPV	negative predictive value
NRI	net reclassification improvement
PA	pleomorphic adenoma

PASL	pulsed ASL
pCASL	pseudo-continuous ASL
PPV	positive predictive value
ROC	receiver operating characteristic
ROI	region of interest
SNR	signal-to-noise ratio
T1WI	T1 weighted image
T2WI	T2 weighted image
TBF	tumor blood flow
TIC	time intensity curve
TSE	turbo spin-echo
WR	washout ratio
WT	Warthin tumor

## Introduction

The most common benign parotid region tumors are pleomorphic adenomas (PA) and Warthin tumors (WT), which together comprise 75–90% of all benign parotid gland tumors [1–4]. The treatment and surgical approach for PAs and WTs of the parotid gland differ. The recommended treatment for WT is enucleation, as it reduces the risk of facial nerve damage [2]. In contrast, patients with PA who were treated with enucleation rather than parotidectomy and patients who had capsular rupture at surgery had higher reported PA recurrence rates [2]. For this reason, PA tumor enucleation is no longer considered an acceptable surgical technique; parotidectomy is the recommended treatment. Therefore, an accurate preoperative diagnosis is necessary to distinguish these tumor types. Thus far, the different patterns of contrast enhancement and the apparent diffusion coefficient (ADC) have been valuable for the differential diagnosis of WTs and PAs in the parotid gland [5–14].

Arterial spin labeling (ASL) is a perfusion imaging technique that uses the intrinsic spin state of arterial blood water as a tracer. This perfusion method has been applied to diagnose and monitor the treatment of central nervous system (CNS) tumors [15–18]. Although the use of ASL perfusion magnetic resonance imaging (MRI) beyond the CNS has been increasing in recent years [19], it still remains unclear whether ASL can provide accurate measurements of tumor blood flow (TBF) in parotid gland tumors. Reports of ASL perfusion findings of parotid gland tumors are limited, though two papers focusing on this topic have been published recently [20, 21], and the applicability of quantitative assessment to WT and PA has not yet been fully clarified. Although our previous study showed that pseudo-continuous ASL (pCASL) may provide a correct evaluation of tumor perfusion of a salivary gland tumor that includes a submandibular gland tumor based on the significant correlation between ASL-TBF and microvessel density (MVD) [20], it did not suffice for the comparison with the conventional MR methods. The current

study included only subjects with parotid gland tumors; we also added a visual assessment of pCASL images and a comparison of the ability of differential diagnosis between pCASL-MRI and the conventional MR methods to this study.

The purposes of this study were as follows: (i) to investigate the correlation between TBF and histopathologic features of WTs and PAs to determine the value of TBF in the differential diagnosis of parotid gland tumors and (ii) to investigate how well pCASL-MRI can qualitatively and quantitatively distinguish PAs from WTs compared to a conventional method.

## Materials and methods

### Subjects

This retrospective study was approved by the institutional review board with a waiver of written informed consent. From April 2011 to July 2014, 23 patients with 10 WTs and 13 PAs of the parotid gland detected by preoperative MRI in our institution were enrolled in this study. One cystic WT was also included in the study (Fig. 1).

All patients underwent routine head and neck MRI and pCASL-MRI. There was no stenosis in the carotid arteries of any patient. pCASL-MR images were acquired for all cases. Because of strong artifact by the artifact due to dental metal, the case that pCASL-MR image was not obtained was not included in this study. Patient demographics are shown in Table 1.

### Conventional MRI protocols

Routine and perfusion MRI scans were performed using a 3T-MR unit (Discovery MR750; GE Healthcare, Waukesha, WI,

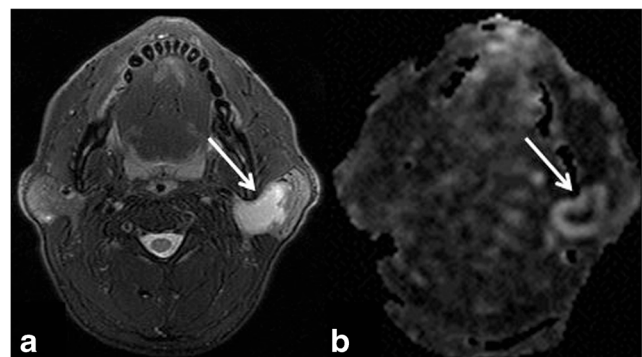


**Fig. 1** A 64-year-old man with a palpable mass in the left parotid gland. Pathological examination of the surgically resected specimen confirmed the diagnosis of a cystic Warthin tumor. **a** Fat suppression T2-weighted image (T2WI) shows a hyperintense tumor in the left parotid gland (arrow). The wall of this tumor is thick and has intermediate signal intensity. **b** pCASL-MR image shows a peripheral hyperintense tumor (arrow); the center signal is dark

**Table 1** Patient demographic

	WT	PA	<i>p</i> value
Sex (M/F)	10:0	11:2	0.21
Age (year)	50–76	31–81	0.03*
Median	62	45	
Diameter (mm)	11.9–37.8	8.2–52.6	0.80
Median	22.2	24.2	

WT Warthin tumor, PA pleomorphic adenoma

\**p* < 0.05

USA) with a 16-channel 3 T Head Neck Spine Array Coil. Axial diffusion-weighted single-shot spin-echo echo planar sequences with fat suppression by using short-tau inversion recovery were acquired using the following parameters: *b* value = 0 and 1000 s/mm<sup>2</sup>; TR/TE/TI = 3600/50.6/248 ms; section thickness/gap = 4 mm/1 mm; field of view (FOV) = 220 mm; matrix size = 220 × 178; number of excitation (NEX) = 1. ADC maps were automatically generated. Dynamic contrast-enhanced MR images were acquired by 3D fat suppression T1-weighted liver acquisition with volume acceleration flexible (LAVA-FLEX) with the following parameters: TR/TE = 5.2/1.8 ms; section thickness/gap = 3.4/–1.7 mm; FOV = 220 × 176 mm; matrix size = 256 × 256; NEX = 0.71. Gd-DTPA (Magnevist; Bayer, Osaka, Japan) was administered (0.1 mmol/kg body weight) at a rate of 2.0 mL/s, and then, a 20-mL saline flush was delivered into the antecubital vein. Dynamic contrast-enhanced T1WI acquisition was performed immediately after intravenous contrast material injection. The scans were sequentially obtained before and 30, 60, 90, 120, 150, 180, and 300 s after contrast material administration.

### ASL perfusion MRI protocols

A 3D spiral fast spin-echo (FSE) sequence with background suppression covering the entire brain was used for pCASL perfusion imaging. A pseudo-continuous scheme was employed for ASL [22]. The parameters for the pCASL perfusion images were as follows: TR/TE = 4700/10.5 ms, spiral readout of 7 arms × 512 samples, 30 to 40 × 4 mm axial sections, and reconstructed pixel size of 1.8 × 1.8 mm. Two averages of label and control pairs required a total time of 2 min and 49–52 s. The position of the labeling plane was located 2 cm below the lowest imaging slices.

For blood flow quantification, an approximate proton density-weighted image was obtained with the same acquisition parameters, except that neither background suppression nor labeling were used. Quantification was performed using the model defined by Alsop and Detre [23] with the inclusion of a term for finite labeling duration [24].

Blood flow was described by the following equation:

$$\text{blood flow} = \lambda \left( 1 - e^{-T_{sat}/T1_g} \right) \times \frac{e^{w/T1_b}}{2\alpha T1_b (1 - e^{-\tau/T1_b})} \times (S_{ctrl} - S_{lbl}) / S_{ref},$$

where labeling time ( $\tau$ ) = 1.5 s, post-label delay ( $w$ ) = 1.5 s, brain–blood partition coefficient ( $\lambda$ ) = 0.9 [25], labeling efficiency ( $\alpha$ ) = 0.8 × 0.75 (pseudo-continuous ASL × background suppression) [26], T1 of blood ( $T1_b$ ) = 1.6 s, saturation recovery time for proton density-weighted image ( $T_{sat}$ ) = 2.0 s, and correction for saturation recovery on proton-density-weighted image ( $T1_g$ ) = 1.2 s.  $S_{ctrl}$  and  $S_{lbl}$  are the signal of the control and label image, respectively, and  $S_{ref}$  is the proton density-weighted reference image. As for calculating TBF, we used the same model and conditions as those used for calculating blood flow in the CNS.

### Data analysis

All MR images were analyzed based on the consensus opinion of two neuroradiologists (TY, 21 years of experience and HK, 28 years of experience). Because the ASL image depicts a signal depending on blood flow, hypoperfusion tumor reveals the iso-signal intensity to surrounding tissue, and we could not recognize tumor itself. Thus, because pCASL-MRI does not provide anatomical details of parotid gland tumors, a region of interest (ROI) selection tool was developed that allowed ROI placement on T1WIs and automatic acquisition of TBF values corresponding to the tumor ROI (Fig. 2). The in-house software was created using IDL (IDL 7.0; Exelis Visual Information Solutions, Boulder, CO, USA). Tumor ROIs were manually drawn on T1WIs corresponding to the TBF map. The ROIs were at least 5 mm in size and included all tumor tissue, but excluded the degeneration and hemorrhage by comparison with contrast-enhanced T1WIs. The mean and maximum calculated value within the ROI was defined as

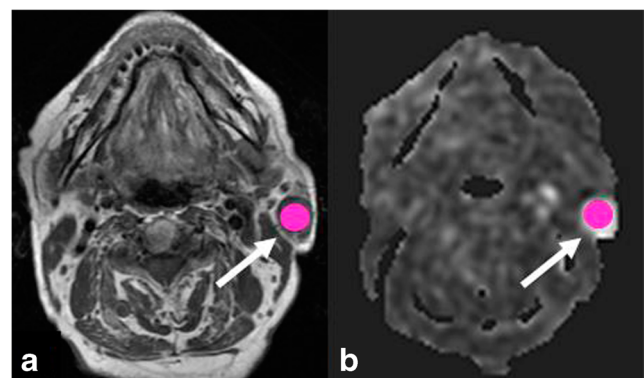


**Fig. 2** Demonstration of ROI placement in a Warthin tumor case. Manually drawn ROI on a T1-weighted image (T1WI) (a) and automatic acquisition of pseudo-continuous arterial spin labeling-tumor blood flow (pCASL-TBF) map (b) corresponding to the tumor ROI

the mean TBF and max TBF. A copy of ROI was placed on the ADC map with calculation of the ADC value of the tumor. The mean calculated value within the ROI on ADC map was defined as the ADC. Three ROI measurements were taken and the results were averaged. A copy of ROI was placed on the T1-weighted dynamic study and time intensity curves (TICs) were constructed. According to the TIC classification that Yabuuchi et al. reported previously [5], we categorized the parotid tumors into four TIC types. In type A, the time to peak ( $T_{peak}$ ) was  $> 120$  s. A parotid gland tumor of this type was considered to have gradual enhancement. In type B, the  $T_{peak}$  was  $\leq 120$  s and the washout ratio (WR) was  $\geq 30\%$ . A parotid gland tumor of this type was considered to have early enhancement and high washout. In type C,  $T_{peak}$  was  $\leq 120$  s and the WR was  $< 30\%$ . A parotid gland tumor with this pattern was considered to have early enhancement and low washout. In type D, the TIC was flat. A parotid gland tumor of this type was considered to be markedly cystic. Visual analysis of the pCASL images was performed using a five-point grading scale (0 = definitely dark signal, 1 = mild low signal, 2 = equivocal (iso-signal to the surrounding parotid gland), 3 = high signal, and 4 = definitely marked high signal). While conducting the analysis, we found that we had to include additional classifications, grade 2 + 0, which we defined as follows: the margin of the tumor has a signal intensity similar to that of the circumference, and the center presents a dark signal, grade 3 + 0, which we defined as follows: the margin of the tumor has a higher signal intensity in the circumference, and the center presents a dark signal. To calculate the sensitivity, specificity, and accuracy of each modality, scores of 3, 4, and 3 + 0 were defined as positive, and scores of 0, 1, 2, and 2 + 0 were regarded as negative. We also compared the TBF calculated from pCASL-MRI and the conventional method with the ADC obtained from diffusion-weighted images (DWIs) and the dynamic-enhanced curve analyses of the two groups. In addition, each method was compared to the pathological results.

### Histopathologic evaluations

We examined microvessel density (MVD) as a histopathologic parameter by immunostaining tissue sections with an antibody against CD34 (Novocastra Laboratories, Newcastle, UK), which identifies vascular endothelial cells. The vessel lumina were recognized as an area surrounded by the CD34-positive endothelial cell layer. Large vessels with thick muscular walls and a lumen of more than approximately 8 red blood cells in diameter were excluded from the count, as described in a previous report [27]. Slides were examined under low-power magnification ( $\times 40$ ) to identify areas with the highest densities of microvessels. In each case, the three most vascularized areas were selected, and digital images were captured with a microscope (PROVIS AX80; Olympus, Tokyo,

Japan) equipped with a digital camera (FX380; Olympus, Tokyo, Japan). A microscopic field of the most intense vascularization in each specimen under a  $\times 200$  field ( $\times 20$  objective and  $\times 10$  ocular,  $0.74 \text{ mm}^2$  per field with the field size measured with an ocular micrometer) was photographed and saved as a JPEG file ( $1600 \times 1200$  pixels, 16.7 million colors, 8-bit). The images were analyzed with MacSCOPE software (Mitani Co., Fukui, Japan) to measure MVD by quantifying the total number of brown staining vessel lumina surrounded by the endothelial cell layer in each field. The histological analyses were performed by an investigator (YI) who was unaware of the pCASL-MRI results. The mean of three counts per tumor was used for the MVD analysis.

### Statistical analysis

The patients' demographics were compared by using Fisher's exact probability test for sex and location, and an unpaired Student's  $t$  test for age and size. MVD, mean and max TBF, and ADC were compared between WTs and PAs using the Mann–Whitney  $U$  test, and  $p < 0.05$  was considered significant. The correlations between MVD and mean and max TBF from pCASL-MRI were evaluated in 10 WTs and 13 PAs by using single linear regression analysis and Spearman's rank correlation coefficients ( $r_s$ ), as well as between MVD and ADC. For the differentiation among these tumors using visual assessment and mean and max TBF, ADC, and TIC, the diagnostic sensitivity, specificity, positive predictive value (PPV), negative predictive value (NPV), and accuracy were calculated with a threshold that was determined by the area under the ROC curve (AUC) using univariate logistic regression analysis based on the histopathologic examination results as the reference standard using statistical software (StatFlex Ver. 6.0; Artech Co., Ltd., Osaka, Japan or The R package; R Development Core Team, Vienna, Austria). The net reclassification improvement (NRI) analysis was used to determine the significance of difference among the AUC of each method [28]. These results were corrected for multiple-comparison testing with the Bonferroni method.

## Results

### Patient demographics

There was a significant difference in age between patients with WT and PA ( $p = 0.03$ ). Other clinical characteristics did not significantly differ between the two types of tumor (Table 1).

### Visual analysis on pCASL-TBF image

We performed a reproducible test of visual analysis with two readers. Interobserver agreement was assessed using the



Cohen kappa statistic and was found to be good ( $\kappa = 0.74$ ). Here, we show one result. In the visual analysis of WT, seven cases were grade 4, one case was grade 3, one case was grade 3 + 0, and one case was grade 1. In the visual analysis of PA, one case was grade 4, one case was grade 2 + 0, and 11 cases were grade 0. The cases with the highest signal intensity were WT and one case of cellular PA. We found that the sensitivity, specificity, and diagnostic accuracy of the visual analysis were 90.0, 92.3, and 91.3%, respectively. Regarding the univariate logistic regression analysis, the AUC was 0.912 for distinguishing between WTs and PAs, and the diagnostic accuracy was 91.3% (Table 2).

**Tumor blood flow**

The mean TBF values were 66.3 to 121.1 mL/100 g/min (median, 95.5 mL/100 g/min) for WT and 11.1 to 86.9 mL/100 g/min (median, 24.5 mL/100 g/min) for PA. The mean TBF was significantly higher in WT than in PA ( $p < 0.01$ ) (Fig. 3). The max TBF values were 88.7 to 224.3 mL/100 g/min (median, 135.2 mL/100 g/min) for WT and 36.8 to 146.1 mL/100 g/min (median, 78.8 mL/100 g/min) for PA. The max TBF was significantly higher in WT than in PA ( $p < 0.01$ ). We show representative cases of WT and PA in Figs. 4 and 5, respectively.

Regarding the ROC curve analysis, when we used a mean TBF of 60.5 mL/100 g/min as the cutoff value to differentiate WTs from PAs, we found that the sensitivity, specificity, PPV, and NPV were 100, 92.3, 90.9, and 100%, respectively. The AUC was 0.969 for distinguishing between WTs and PAs, and the diagnostic accuracy was 95.7% (Table 2).

**ADC**

The ADC values were 0.67 to  $1.49 \times 10^{-3}$  mm<sup>2</sup>/s (median,  $0.85 \times 10^{-3}$  mm<sup>2</sup>/s) for WT and 1.06 to  $2.36 \times 10^{-3}$  mm<sup>2</sup>/s (median,  $1.57 \times 10^{-3}$  mm<sup>2</sup>/s) for PA. ADC was significantly lower in WT than in PA ( $p < 0.01$ ).

Regarding the ROC curve analysis, when we used an ADC of  $1.27 \times 10^{-3}$  mm<sup>2</sup>/s as the cutoff value to differentiate WTs from PAs, we found that the sensitivity, specificity, PPV, and

**Table 2** Diagnostic performance

	Sensitivity	Specificity	PPV	NPV	Accuracy	AUC
Mean TBF	100	92.3	90.9	100	95.7	0.969
Max TBF	90.0	92.3	90.0	92.3	87.0	0.939
Visual	90.0	92.3	90.0	92.3	91.3	0.912
ADC	80.0	92.3	88.9	85.7	87.0	0.889
TIC	77.8	92.3	87.5	85.7	86.4	0.850

TBF tumor blood flow, ADC apparent diffusion coefficient, TIC time intensity curve, PPV positive predictive value, NPV negative predictive value, AUC area under the curve

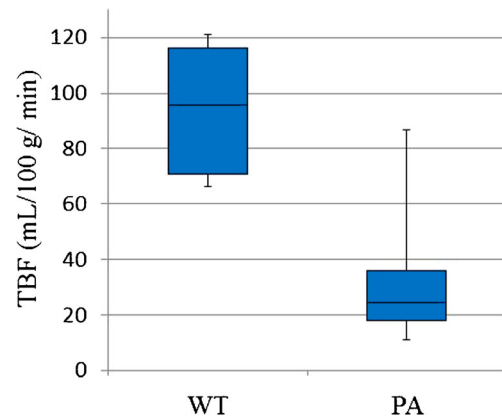


**Fig. 3** Comparison of mean tumor blood flow between Warthin tumors and pleomorphic adenomas. Box-and-whisker plots show tumor blood flow (TBF) measurements in Warthin tumors (WT) and pleomorphic adenomas (PA). The lower and upper hinges of the boxes denote the 25th and 75th percentiles, respectively. The median (50th percentile) of each distribution is indicated by the line. Whiskers on either side extend to the most extreme data point. Note the significant difference between WTs and PAs ( $p < 0.01$ ) for TBF, WT Warthin tumor, PA pleomorphic adenoma, TBF tumor blood flow

NPV were 80.0, 92.3, 88.9, and 85.7%, respectively. The AUC was 0.889 for distinguishing between WTs and PAs, and the diagnostic accuracy was 87.0% (Table 2).

**TIC pattern**

All patients underwent dynamic contrast enhanced study, except one WT patient with renal dysfunction. Of the 9 WTs, 7 (77.8%) were type B curve and two was a type C. Twelve of the thirteen PAs were type A, but one was a type B, which was a cellular PA. Regarding the univariate logistic regression analysis, the AUC was 0.85 for distinguishing between WTs and PAs, and the diagnostic accuracy was 86.4% (Table 2).

**MVD**

The MVD were between 115 and 301 (median, 133) for WT and between 20 and 80 (median, 29) for PA. MVD was significantly higher in WT than in PA ( $p < 0.01$ ) (Fig. 6).

**Comparison among each AUC**

According to the NRI analysis, there were significant differences between the AUC of mean TBF and the AUCs of ADC, TIC, and visual assessment ( $p < 0.005$ , respectively) (Table 3). There was no significant difference among other methods. It was judged that the mean TBF was superior to the other methods such as ADC, TIC, and visual assessment in differentiating WTs from PAs.

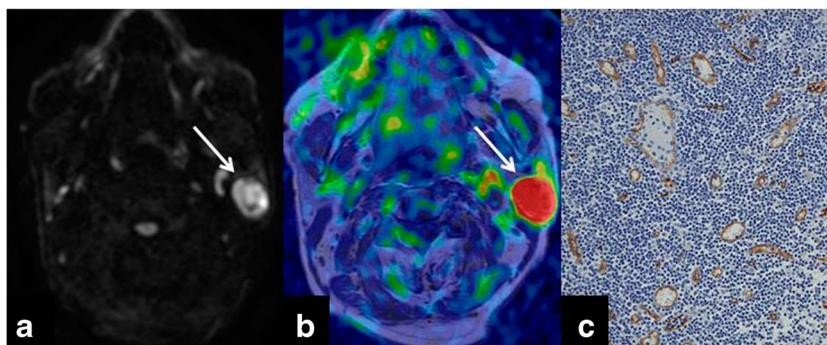


**Fig. 4** A 70-year-old man with a swollen left parotid gland. Pathological examination of the surgically resected specimen confirmed the diagnosis of Warthin tumor. **a** Diffusion weighted image (DWI) shows a bright, hyperintense tumor in the left parotid gland (arrow). **b** The fusion image (pCASL-MR image, color scale, and T1-weighted post-contrast MR

imaging, gray scale) shows a red signal that overlaps the tumor (arrow), suggesting elevated TBF (91.7 mL/100 g/min). **c** Immunohistochemical staining for CD34 reveals brown-stained microvessels on a blue tumor cell background; the microvessel density is 126 counts/microscopic high-power magnification field

### Linear regression analyses

Correlation analyses revealed a strong positive correlation between MVD and mean TBF in all tumors ( $r_s = 0.93$ ,  $R^2 = 0.84$ ,  $p < 0.01$ ) (Fig. 7). Correlation analyses revealed a strong positive correlation between MVD and max TBF in all tumors ( $r_s = 0.89$ ,  $R^2 = 0.70$ ,  $p < 0.01$ ). Correlation analyses revealed a weak negative correlation between MVD and ADC in all tumors ( $r_s = 0.56$ ,  $R^2 = 0.28$ ,  $p < 0.01$ ).

### Discussion

In the current study, we evaluated the ability of pCASL perfusion MR imaging to differentiate between two common parotid gland tumor types on the basis of qualitative and quantitative assessments. Using pCASL-MR images, we performed visual analyses, as well as measurements of TBF. We were able to qualitatively and immediately differentiate WTs from PAs in a clinical setting based on visual assessment of the pCASL-MR images. Furthermore, using histopathological results as a reference standard, we found a significant

correlation between TBF, as measured by pCASL-MRI, and MVD on histological specimens.

The accurate diagnosis of parotid gland tumors is critical for the planning of surgical treatment and an accurate prognosis. Before surgery, MRI is typically performed for tumor type diagnosis and an assessment of the tumor extension surrounding the parotid gland. Although MRI allows visualization of the tumor extension and peri-glandular complex anatomy, it is still difficult to histologically differentiate parotid gland tumors without aspiration cytology.

There have been a few studies that applied ASL-MRI to parotid gland tumors [20, 21]. WTs had high signal intensity in this study, and the opposite was observed in the PAs, except for one cellular pleomorphic adenoma. This shows that a simple visual inspection of pCASL-MR images could provide direct differential diagnosis without the need for quantitative measurements in a clinical setting. This is very consistent with the result demonstrating that the TBF was significantly higher in WTs than in PAs. Using the cutoff value of mean TBF of 60.5 mL/100 g/min, we could discriminate WTs from PAs with an accuracy of 95.7%. The accuracy of the TBF was higher than the ADC (87%). We could also readily

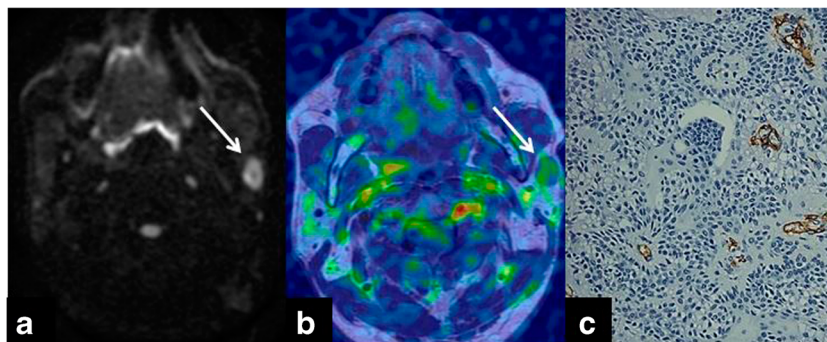


**Fig. 5** A 63-year-old man with a palpable mass in the left parotid gland. Pathological examination of the surgically resected specimen confirmed the diagnosis of pleomorphic adenoma. **a** DWI reveals a hyperintense tumor in the left parotid gland (arrow). **b** The fusion image (pCASL-

MR image and T1-weighted post-contrast MR imaging) shows hypointensity (arrow), suggesting low TBF (11.1 mL/100 g/min). **c** CD34 staining of the microvessels yielded a microvessel density of 20 counts/microscopic high-power magnification field

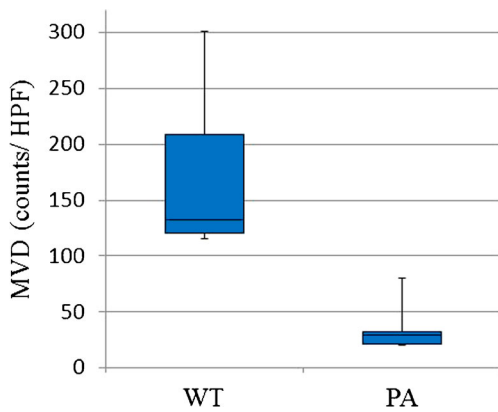


**Fig. 6** Comparison of microvessel density in Warthin tumors and pleomorphic adenomas. Box-and-whisker plots show the distribution of microvessel density (MVD) in Warthin tumors and pleomorphic adenomas. The lower and upper hinges of the boxes denote the 25th and 75th percentiles, respectively. The median (50th percentile) of each distribution is indicated by the line. Whiskers on either side extend to the most extreme data point. A significant difference in MVD is observed between these tumor types ( $p < 0.01$ ), WT Warthin tumor, PA pleomorphic adenoma, MVD microvessel density, HPF high-power magnification field

differentiate these tumors visually using ASL-MRI, and the utility value of ASL-MRI was high. The mean TBF was significantly superior to the other methods such as ADC, TIC, and visual assessment in differentiating WTs from PAs. Liu et al. reported that the cerebral blood flow (CBF) was higher in young women than young men, and there was no significant difference between old men and young men [29]. Although this study was not a study of the CBF, we think that differences in age and sex would not influence the TBF measurements even if we applied their results, as the WT with a high TBF is older than PA, and WT patients are almost all male.

**Table 3** Comparison among each AUC

	NRI	P value
Mean vs. max	-0.6496 (-1.2418 to -0.0573)	0.0316
Mean vs. ADC	-0.7863 (-1.3288 to -0.2439)	0.0045*
Mean vs. TIC	-1.3248 (-1.7757 to -0.8739)	0*
Mean vs. visual	-0.9744 (-1.4731 to -0.4756)	0.0001*
Max vs. ADC	-0.5641 (-1.2153-0.0871)	0.0895
Max vs. TIC	-0.0855 (-0.7315-0.5606)	0.7954
Max vs. visual	-0.0855 (-0.6534-0.4824)	0.7680
ADC vs. TIC	-0.1197 (-0.7683-0.5290)	0.7177
ADC vs. visual	-0.1197 (-0.6905-0.4512)	0.6812
Visual vs. TIC	-0.1111 (-0.4813-0.2590)	0.5563

NRI net reclassification improvement, mean mean tumor blood flow, max max tumor blood flow

Other abbreviations as in Table 2

Data in parentheses are 95% confidence intervals

\*Difference was significant ( $P < .005$ )

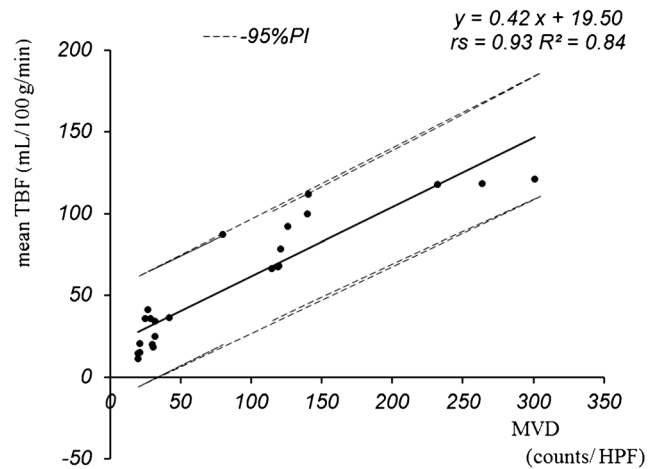


**Fig. 7** Linear regression graphs showing the correlation between microvessel density and tumor blood flow for all tumors. Scatter plots of the microvascular density (MVD) with respect to the measured tumor blood flow (TBF) in 23 parotid gland tumors are shown. The regression line with 95% PI lines is shown ( $y = 0.42x + 19.50$ , where x indicates the MVD and y indicates the mean TBF:  $r_s = 0.93$ ;  $R^2 = 0.84$ ,  $p < 0.01$ ). Note the positive correlation between the MVD and the TBF, HPF high-power magnification field, TBF tumor blood flow, PI predict interval

Furthermore, the MVD was also significantly higher in WTs than in PAs; according to our histological examination, WT was confirmed to be a vascular-rich tumor, which is in agreement with a previous report [5, 30]. In this study, there was a positive correlation between a quantitative value (TBF) and the number of microvessels (MVD), which indicates that TBF measurements via pCASL-MRI could be used to evaluate tumors of the parotid gland. The correlation between the number of the microvessels and TBF was previously reported for brain tumors, and we previously reported that there was a positive correlation between TBF and the number of the microvessels for meningioma [15, 31]. Noguchi et al. also reported a positive correlation between TBF and the microvessels of brain tumors (e.g., lymphoma and high-grade glioma) [16]. Although there are several reports in brain tumors as above, it may also be worth mentioning that the confirmation was successful even when tumors were located in the parotid gland region.

One of the previous attempts to distinguish parotid gland tumors was based on the characteristics of tumor enhancement visualized on post-contrast MRI. The cumulative prolonged and delayed enhancement after about 5-min post-contrast material injection has been reported as a characteristic finding of PA [5–9], except in some tumors that were full of epithelial components. On the other hand, WT showed an enhancement pattern of rapid increase and decrease, and an early peak time (within 120 s) and high wash out ratio (more than 30%) have been reported as characteristic to WT [5–8]. The opposite pattern of the contrast enhancement in PA may be closely related to the underlying mechanism of hyperperfusion of ASL-MRI that is predominantly observed in WT cases. As



for the TICs in our cases, there was a lot of type B (77.8%, early contrast enhancement) in WT and type A (92.3%, gradually contrast enhancement) in PA, which agrees with the report of Yabuuchi et al. [5]. WT is characterized by early contrast enhancement, corresponding to hyperperfusion in pCASL-MRI; on the other hand, PA is characterized by gradually contrast enhancement, corresponding to hypoperfusion in pCASL-MRI. It may be a challenge for ASL imaging to visualize perfusion state with very slow flow such as late phase dynamic contrast enhancement, since the label effect of ASL is limited to a short time.

Another attempt to categorize parotid gland tumors using MRI features is the evaluation of diffusion characteristics. There have been many studies attempting differential diagnosis based on an ADC value measured by DWI [10–14]. Although the acquisition parameters of the DWI varied among these reports, one common finding was that WT had the lowest ADC value among the assessed tumor types, besides malignant lymphoma, which reflects a rich lymphoid tissue-related interstitium [5]. In contrast, PA had the highest ADC value, which reflects an abundant myxoma-like stroma [5]. There is an overlap between the ADC values of benign tumor and malignant tumor, i.e., ADC values alone are insufficient for accurate diagnosis, and other imaging findings are generally required. There are some reports of the diagnostic utility of combining DWI with an evaluation of tumor hemodynamics by multi-phase CT/MR [10, 11, 32]. Kato et al. reported that a combined usage of ASL-MRI and ADC was helpful in the differentiation of parotid gland tumors [21]. Although Takumi et al. recently reported that they can distinguish PA from WT using fractional anisotropy measurement based on diffusion tensor imaging as an application of DWI [33], the technique cannot visually evaluate those parameters as our study did. Conventional DWI is performed using single-shot echo-planar imaging (EPI), which is rapid and provides a good signal-to-noise ratio (SNR). However, the use of this technique in local magnetic field inhomogeneities can increase image distortion by centimeters. Mikayama et al. reported that turbo spin-echo (TSE)-DWI had significantly decreased image distortion and an increased SNR in the head and neck region compared to EPI-DWI [34]. In general, the TSE sequence, which obtains echo by refocusing RF pulses, is less sensitive to susceptibility artifacts than a conventional EPI sequence [35]. Reduced image distortion may provide better reproducibility and reliability of DWI and the quantitative parameters [36].

Until now, the two most successful methods for differential diagnosis of parotid gland tumors have been the enhancement pattern after administration of contrast material and ADC values obtained by DWI, which may increase invasiveness and complexity. However, the pCASL-MRI technique used in this study can obtain information about tumor perfusion without radiation exposure or the administration of contrast

material. In pulsed ASL (PASL), a different ASL technique, SNR, is lower than pCASL. pCASL is higher in label efficiency than PASL and is more stable. pCASL sequences have used 3D-FSE acquisition, which is less susceptible to artifact than echo-planar imaging-based ASL sequences [37]. Therefore, pCASL is suitable for imaging of the head and neck regions. Moreover, our findings suggest that the two most common types of parotid gland tumors can be distinguished promptly and accurately with pCASL-MRI, showing that it is suitable for evaluating whether intensity of the tumor is high or low, and it is worth adding as a routine protocol.

Although our primary interest is to differentiate benign and malignant parotid tumors, there are few malignant cases, and none were included in this examination. TBF values measured by pCASL-MRI for malignant parotid tumors are overlapped with either WT or PA in limited experience of our small group; there was not a significant difference in TBF between patients with malignant tumor and these two types of tumors. WTs could potentially be watched, and PAs and malignant tumors could be resected. It would be helpful to compare WTs to PAs and malignant tumors, as previously reported by Kato et al. Although ASL-MRI cannot completely replace fine-needle aspiration, it is non-invasive and simple, and we think it will play an important role in the selection of treatment methods.

The results of this study must be evaluated in the light of its limitations. First, the small sample size may limit extrapolation of these findings beyond the current sample. Second, we could not accurately co-register MR images with pathological specimens. This means that the number of microvessels detected by the histopathological analysis does not necessarily precisely represent the TBF value measured by the ROI placed on the tumor. Third, there is an absence of harmonization of ASL techniques among manufacturers. Therefore, the use of a different ASL sequence may not guarantee reproducibility. In addition, ASL-MRI has the faults of a low SNR, limited spatial resolution. Lastly, it was difficult to differentiate the cellular PA from WT using pCASL-TBF because the MVD of the cellular PA was high, similar to WT. Therefore, ASL-TBF measurements, taken by themselves, could be misleading in cases of cellular PA. The precise frequency of cellular PA has not reported, and there are only a few case reports [38, 39]. However, it was reported that cellular PA had a lower frequency of recurrence than myxoid-rich PA [2]. Cellular PA seems to be a rare histological subtype of PA [40]. Finally, the relative lack of cystic WTs in the study population may have been a potential limitation, although only one case of cystic WT indicated peripheral hyperintensity on pCASL-MR images. In spite of these limitations, we believe that our current results prove that pCASL-MR images have a high diagnostic value for the identification of WTs.



## Conclusions

The values of TBF measured by pCASL-MRI were significantly higher in WTs than in PAs, based on quantitative assessment, and there was a positive correlation between TBF and MVD. Furthermore, we were able to qualitatively differentiate WTs from PAs based on visual assessment of ASL perfusion images in a clinical setting. pCASL-MRI provides more accurate imaging to differentiate WTs from PAs than conventional imaging such as ADC or TIC assessment.

## Compliance with ethical standards

**Funding** This study was funded in part by Grants-in-Aid for Scientific Research (C) (15k09916) from the Japan Society for the Promotion of Science (HK).

**Conflict of interest statement** The authors declare that they have no conflict of interest.

**Ethical standards** We declare that all human and animal studies have been approved by the University of Fukui Ethics Committee and have therefore been performed in accordance with the ethical standards laid down in the 1964 Declaration of Helsinki and its later amendments. For this type of study formal consent is not required.

**Informed consent** For this type of retrospective study formal consent is not required.

## References

- Shimizu M, Ussmuller J, Hartwein J et al (1999) Statistical study for sonographic differential diagnosis of tumorous lesions in the parotid gland. *Oral Surg Oral Med Oral Pathol Oral Radiol Endod* 88:226–233
- Som PM, Brandwein-Gensler MS (2011) Anatomy and pathology of the salivary gland, epithelial tumors. In: Som PM, Curtin HD (eds) *Head and neck imaging*, 5th edn. Mosby, St Louis, pp 2525–2544
- Wittich GR, Scheible WF, Hajek PC (1985) Ultrasonography of the salivary glands. *Radiol Clin N Am* 23:29–37
- Zajkowski P, Jakubowski W, Białek EJ, Wysocki M, Osmólski A, Serafin-Król M (2000) Pleomorphic adenoma and adenolymphoma in ultrasonography. *Eur J Ultrasound* 12:23–29
- Yabuuchi H, Fukuya T, Tajima T, Hachitanda Y, Tomita K, Koga M (2003) Salivary gland tumors: diagnostic value of gadolinium-enhanced dynamic MR imaging with histopathologic correlation. *Radiology* 226:345–354
- Ikeda M, Motoori K, Hanazawa T, Nagai Y, Yamamoto S, Ueda T, Funatsu H, Ito H (2004) Warthin tumor of the parotid gland: diagnostic value of MR imaging with histopathologic correlation. *AJNR Am J Neuroradiol* 25:1256–1262
- Yerli H, Aydin E, Coskun M, Geyik E, Ozluoglu LN, Haberal N, Kaskati T (2007) Dynamic multislice computed tomography findings for parotid gland tumors. *J Comput Assist Tomogr* 31:309–316
- Hisatomi M, Asaumi J, Yanagi Y, Unetsubo T, Maki Y, Murakami J, Matsuzaki H, Honda Y, Konouchi H (2007) Diagnostic value of dynamic contrast-enhanced MRI in the salivary gland tumors. *Oral Oncol* 43:940–947
- Christe A, Waldherr C, Hallett R, Zbaeren P, Thoeny H (2011) MR imaging of parotid tumors: typical lesion characteristics in MR imaging improve discrimination between benign and malignant disease. *AJNR Am J Neuroradiol* 32:1202–1207
- Yabuuchi H, Matsuo Y, Kamitani T, Setoguchi T, Okafuji T, Soeda H, Sakai S, Hatakenaka M, Nakashima T, Oda Y, Honda H (2008) Parotid gland tumors: can addition of diffusion-weighted MR imaging to dynamic contrast-enhanced MR imaging improve diagnostic accuracy in characterization? *Radiology* 249:909–916
- Eida S, Sumi M, Nakamura T (2010) Multiparametric magnetic resonance imaging for the differentiation between benign and malignant salivary gland tumors. *J Magn Reson Imaging* 31:673–679
- Habermann CR, Arndt C, Graessner J, Diestel L, Petersen KU, Reitmeier F, Ussmuller JO, Adam G, Jaehne M (2009) Diffusion-weighted echo-planar MR imaging of primary parotid gland tumors: is a prediction of different histologic subtypes possible? *AJNR Am J Neuroradiol* 30:591–596
- Eida S, Sumi M, Sakihama N, Takahashi H, Nakamura T (2007) Apparent diffusion coefficient mapping of salivary gland tumors: prediction of the benignancy and malignancy. *AJNR Am J Neuroradiol* 28:116–121
- Matsushima N, Maeda M, Takamura M, Takeda K (2007) Apparent diffusion coefficients of benign and malignant salivary gland tumors. Comparison to histopathological findings. *J Neuroradiol* 34:183–189
- Kimura H, Takeuchi H, Koshimoto Y, Arishima H, Uematsu H, Kawamura Y, Kubota T, Itoh H (2006) Perfusion imaging of meningioma by using continuous arterial spin-labeling: comparison with dynamic susceptibility-weighted contrast-enhanced MR images and histopathologic features. *AJNR Am J Neuroradiol* 27:85–93
- Noguchi T, Yoshiura T, Hiwataishi A, Togao O, Yamashita K, Nagao E, Shono T, Mizoguchi M, Nagata S, Sasaki T, Suzuki SO, Iwaki T, Kobayashi K, Mihara F, Honda H (2008) Perfusion imaging of brain tumors using arterial spin-labeling: correlation with histopathologic vascular density. *AJNR Am J Neuroradiol* 29:688–693
- Weber MA, Thilmann C, Lichy MP et al (2004) Assessment of irradiated brain metastases by means of arterial spin-labeling and dynamic susceptibility-weighted contrast-enhanced perfusion MRI: initial results. *Investig Radiol* 39:277–287
- Yamamoto T, Kinoshita K, Kosaka N, Sato Y, Shioura H, Takeuchi H, Kimura H (2013) Monitoring of extra-axial brain tumor response to radiotherapy using pseudo-continuous arterial spin labeling images: preliminary results. *Magn Reson Imaging* 31:1271–1277
- Shimizu K, Kosaka N, Fujiwara Y, et al (2016) Arterial transit time-corrected renal blood flow measurement with pulsed continuous arterial spin labeling MR imaging. *Magn Reson Med Sci* 2016 May 9
- Yamamoto T, Kosaka N, Mori M, Imamura Y, Kimura H (2014) Assessment of tumor blood flow and its correlation with histopathologic features in Warthin tumors and pleomorphic adenomas of the salivary gland by using pulsed-continuous arterial spin labeling images. In: *Proceedings of the Joint Annual Meeting ISMRM-ESMRMB*, Milan, Italy
- Kato H, Kanematsu M, Watanabe H, Kajita K, Mizuta K, Aoki M, Okuaki T (2015) Perfusion imaging of parotid gland tumours: usefulness of arterial spin labeling for differentiating Warthin's tumours. *Eur Radiol* 25:3247–3254
- Dai W, Garcia D, de Bazelaire C, Alsop DC (2008) Continuous flow-driven inversion for arterial spin labeling using pulsed radio frequency and gradient fields. *Magn Reson Med* 60:1488–1497
- Alsop DC, Detre JA (1996) Reduced transit-time sensitivity in non-invasive magnetic resonance imaging of human cerebral blood flow. *J Cereb Blood Flow Metab* 16:1236–1249

24. Wang J, Zhang Y, Wolf RL, Roc AC, Alsop DC, Detre JA (2005) Amplitude-modulated continuous arterial spin-labeling 3.0-T perfusion MR imaging with a single coil: feasibility study. *Radiology* 235:218–228
25. Herscovitch P, Raichle ME (1985) What is the correct value for the brain - blood partition coefficient for water? *J Cereb Blood Flow Metab* 5:65–69
26. Garcia DM, Duhamel G, Alsop DC (2005) Efficiency of inversion pulses for background suppressed arterial spin labeling. *Magn Reson Med* 54:366–372
27. Bosari S, Lee AK, DeLellis RA et al (1992) Microvessel quantitation and prognosis in invasive breast carcinoma. *Hum Pathol* 23:755–761
28. Pepe MS, Fan J, Feng Z, Gerds T, Hilden J (2015) The net reclassification index (NRI): a misleading measure of prediction improvement even with independent test data sets. *Stat Biosci* 7:282–295
29. Liu W, Lou X, Ma L (2016) Use of 3D pseudo-continuous arterial spin labeling to characterize sex and age differences in cerebral blood flow. *Neuroradiology* 58:943–948
30. Woo SH, Choi DS, Kim JP, Park JJ, Joo YH, Chung PS, Kim BY, Ko YH, Jeong HS, Kim HJ (2013) Two-phase computed tomography study of Warthin tumor of parotid gland: differentiation from other parotid gland tumors and its pathologic explanation. *J Comput Assist Tomogr* 37:518–524
31. Yamamoto T, Takeuchi H, Kinoshita K, Kosaka N, Kimura H (2014) Assessment of tumor blood flow and its correlation with histopathologic features in skull base meningiomas and schwannomas by using pseudo-continuous arterial spin labeling images. *Eur J Radiol* 83:817–823
32. Motoori K, Ueda T, Uchida Y, Chazono H, Suzuki H, Ito H (2005) Identification of Warthin tumor: magnetic resonance imaging versus salivary scintigraphy with technetium-99m pertechnetate. *J Comput Assist Tomogr* 29:506–512
33. Takumi K, Fukukura Y, Hakamada H, Ideue J, Kumagae Y, Yoshiura T (2017) Value of diffusion tensor imaging in differentiating malignant from benign parotid gland tumors. *Eur J Radiol* 95:249–256
34. Mikayama R, Yabuuchi H, Sonoda S, Kobayashi K, Nagatomo K, Kimura M, Kawanami S, Kamitani T, Kumazawa S, Honda H (2018) Comparison of intravoxel incoherent motion diffusion-weighted imaging between turbo spin-echo and echo-planar imaging of the head and neck. *Eur Radiol* 28:316–324
35. Sigmund EE, Jensen J (2011) Basic physical principles of body diffusion-weighted MRI. In: Taouli B (ed) *Extra-cranial applications of diffusion-weighted MRI*. Cambridge University Press, Cambridge, pp 1–17
36. Verhappen MH, Pouwels PJ, Ljumanovic R et al (2012) Diffusion weighted MR imaging in head and neck cancer: comparison between half-fourier acquisition single-shot turbo spin-echo and EPI techniques. *AJNR* 33:1239–1246
37. Alsop DC, Detre JA, Golay X, Günther M, Hendrikse J, Hernandez-Garcia L, Lu H, MacIntosh BJ, Parkes LM, Smits M, van Osch MJP, Wang DJJ, Wong EC, Zaharchuk G (2015) Recommended implementation of arterial spin-labeled perfusion MRI for clinical applications: a consensus of the ISMRM perfusion study group and the European consortium for ASL in dementia. *Magn Reson Med* 73:102–116
38. Guerra G, Testa D, Montagnani S, Tafuri D, Salzano FA, Rocca A, Amato B, Salzano G, Dell'Aversana Orabona G, Piombino P, Motta G (2014) Surgical management of pleomorphic adenoma of parotid gland in elderly patients: role of morphological features. *Int J Surg* 12(Suppl 2):S12–S16
39. Ananthaneni A, Undavalli SB (2013) Juvenile cellular pleomorphic adenoma. *BMJ Case Rep* 2013:bcr2012007641. <https://doi.org/10.1136/bcr-2012-007641>
40. McGregor AD, Burgoyne M, Tan KC (1988) Recurrent pleomorphic salivary adenoma—the relevance of age at first presentation. *Br J Plast Surg* 41:177–181